DESIGN AND CONSTRUCTION OF A SCANNING TUNNELING MICROSCOPE FOR THE STUDY OF THIN METAL FILMS

By

Nathan Tyler

A thesis submitted in partial fulfillment of the
requirements for the degree of

Bachelor of Science

Houghton University

May 2026

Signature of Author……………………………………………………………………………………..
Department of Physics
May 6, 2026

………
Dr. Brandon Hoffman
Professor of Physics
Research Supervisor

………
Dr. Mark Yuly
Professor of Physics

DESIGN AND CONSTRUCTION OF A SCANNING TUNNELING MICROSCOPE FOR THE STUDY OF THIN METAL FILMS

By

Nathan Tyler

Submitted to the Department of Physics
on May 6, 2026 in partial fulfillment of the
requirement for the degree of
Bachelor of Science

Abstract

Houghton University is building a Scanning Tunneling Microscope (STM) to analyze the surface of thin metal films in air at an atomic resolution. A dual-stage vibration isolation system is used to reduce noise. Stepper motors move the scanning head toward the sample surface, after which a piezo buzzer scans a tip across the surface while adjusting the height to maintain a constant current. The position of the tip is therefore an image of the surface. All the electronics are controlled by a Teensy 4.1 microcontroller. The hardware, electronics, and software have been successfully tested independently of one another, but not yet as a complete system.

Thesis Supervisor: Dr. Brandon Hoffman
Title: Professor of Physics

TABLE OF CONTENTS

TABLE OF FIGURES

Chapter 1

FUNDAMENTALS OF SCANNING PROBE MICROSCOPY

1.1. Scanning Tunneling Microscopy

Scanning probe microscopy (SPM) [1] is a family of techniques used to study surface structure. These techniques operate by using a sharp probe to scan across a surface and measure what happens between the probe and the surface of the sample. By measuring this interaction as a function of position, detailed images of surface and crystalline structure are obtained. Since different physical interactions between the tip and sample can be detected, SPM includes several variations, each offering specific advantages and drawbacks.

Each type of SPM is distinguished by the physical interaction that it measures. Atomic force microscopy (AFM) detects short-range interaction forces between the tip and the sample. A benefit of this type of STM is its ability to be used on both conducting and insulating surfaces. However, these interaction forces can sometimes distort the surface itself leading to complications in the sample. Magnetic force microscopy (MFM) measures the magnetic forces between a probe and a sample surface. This allows researchers to study the magnetic properties of materials. Scanning near-field optical microscopy (SNOM) uses a very small probe to measure light from the surface of a sample. This allows scientists to study how materials interact with light at very small scales.

Scanning tunneling microscopes (STM) are used to make atomic resolution images of conducting surfaces [2]. An STM scans an atomically sharp metal tip across the surface of a substrate, as shown in Figure 1.

The first STM [3] was created by Gerd Binnig and Heinrich Rohrer in 1981 at IBM's Zurich Research Laboratory. The STM provided the world with the first three-dimensional atomic level images of surface structure, seen in Figure 2. This represented a major advancement for the surface science, material science, and physics world. The first images that Binnig and Rohrer acquired were those of the surface of silicon. In 1986 Gerd Binnig and Heinrich

Rohrer jointly won the Nobel prize [4] in physics for their work on the STM. They split the prize with Ernst Ruska for his work on the invention of the electron microscope.

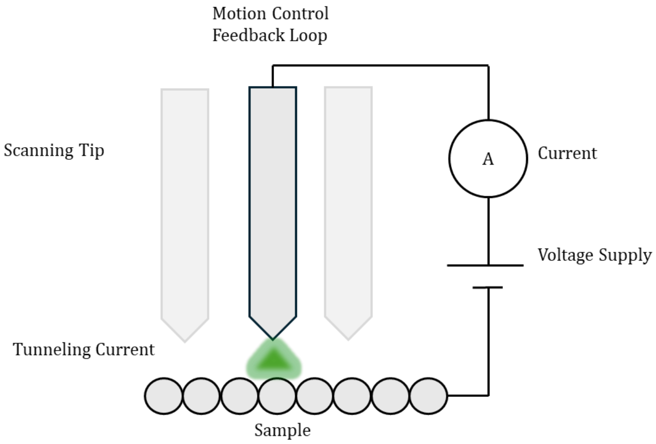

Figure 1. Basic schematic of STM operation showing a sharp tip positioned above a conductive substrate that scans across the surface. The row of spheres represents atoms on the sample surface, while the highlighted area beneath the tip indicates the region where tunneling occurs. When the tip is brought within nanometers of the surface, electron tunneling between the tip and the sample generates a current used to map the atomic structure of the surface.

When designing their STM, Binnig and Rohrer encountered a problem in trying to isolate external vibrations. To achieve little to no vibrations the equipment was situated atop a large rock, supported by multiple inflatable tubes. Eddy currents [5] were also used to dampen and reduce the amount of vibrations present. Eddy current damping occurs when a conductor moves through a magnetic field, as shown in Figure 3. The changing magnetic flux through the conductor induces an electromotive force (emf), generating circulating currents known as eddy currents. These currents interact with the magnetic field to produce a Lorentz force that opposes the motion, thereby damping the vibrations in the system.

After mechanical vibrations are minimized through eddy current damping, the STM can image the substrate surface. STM imaging is performed in one of two configurations, as seen in Figure 4: constant-height mode and constant-current mode. In constant-height mode, the tip–sample distance (defined as the vertical position of the tip relative to the sample stage) is fixed and the tunneling current is measured as a function of position. In constant-current mode, the tunneling current is kept constant by adjusting the tip–sample distance, and the tip height is measured as a function of position. In either case, the measured signal produces an intensity map comparable to a topographic image of the surface. Binnig and Rohrer demonstrated this capability by obtaining the atomic-resolution image of platinum clusters deposited on a graphite substrate in Figure 5.

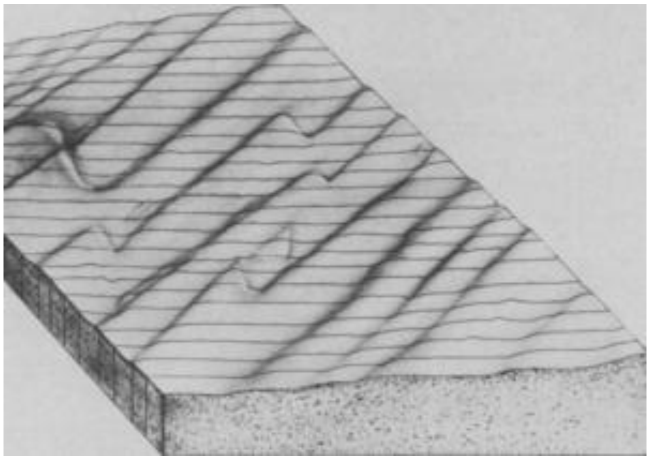

Figure 2. STM topographic image of a Si(111) surface showing flat terraces separated by step lines about 3 Å high. The steps correspond to single atomic layers of silicon and were measured using scanning tunneling microscopy, developed by Binnig and Rohrer. Figure taken from Ref. [2].

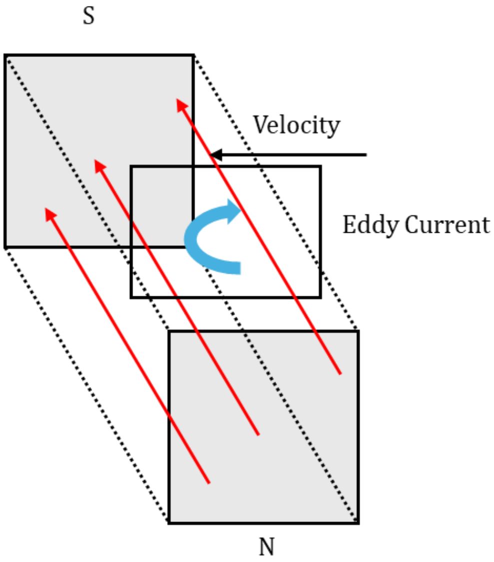

Figure 3. Eddy currents (blue arrow) produces a magnetic flux in the metal that opposes a change in the total magnetic flux due to the metal moving through the external magnetic field (red arrows). The result is a force opposite the velocity. Diagram adapted from Ref. [5].

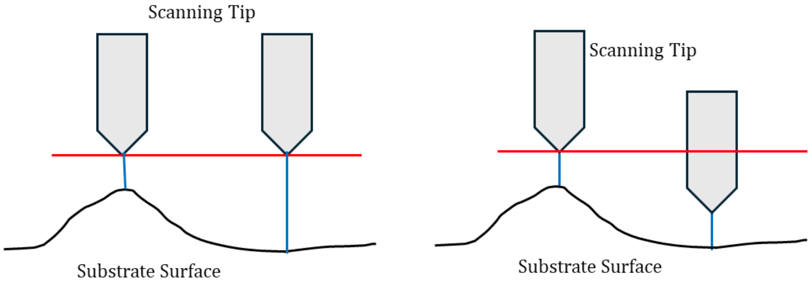

Figure 4. Comparison of constant-current and constant-height scanning modes in STM . In constant-height mode (left), the tip height (red) remains fixed while current variations (blue) reflect surface features. In constant-current mode (right), the tip height (red) adjusts to maintain a steady tunneling current (blue).

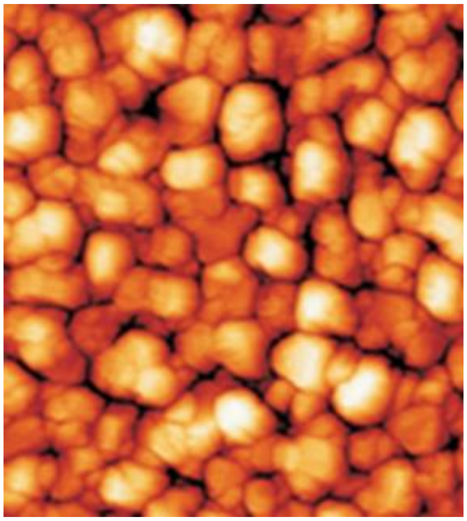

Figure 5. STM image of Platinum nanoparticles on a graphite substrate. The bright spots are the Pt clusters distributed across the graphite surface (10 nm x 10 nm). Figure taken from Ref. [2].

1.2. *STM Imaging in a Vacuum*

Early in the development of the STM, there was uncertainty about whether the images were caused by electron tunneling or by physical contact between the tip and the sample. In a 1990 study [6] completed by R. Wiesendanger and H.-J. Güntherodt, researchers used an STM that was operated in an ultra-high vacuum to closely look at the electron tunneling that occurred between a sharp tip and a clean single-crystalline chromium surface shown in Figure 6. By imaging the Cr(001) surface in ultra-high vacuum, the experiment demonstrated that image contrast arises from variations in the tunneling current across the vacuum gap.

Because a tunneling current can only occur when the tip and sample are separated by a small distance without physical contact, the successful acquisition of a detailed surface image in this experiment supports that the STM is operating in the expected quantum tunneling rather than through tip–surface contact. This now made it possible to connect tunneling current to the atomic arrangement and electronic properties of single crystalline materials in a vacuum.

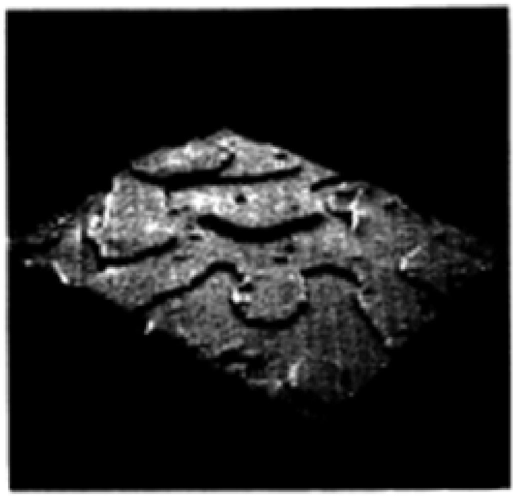

Figure 6. Constant current STM image obtained in vacuum demonstrating terraces separated by irregular monatomic step edges on a single crystalline surface, (32 nm x 32 nm). Figure taken from Ref. [6].

In a later study, Holger Wolfschmidt [7] used an STM to look at the atomic structure of well-defined single-crystalline metal surfaces as shown in Figure 7. In this image the terracing and monatomic step edges were able to be seen. Because single crystals have a regular atomic structure, the tunneling current changed in a consistent and predictable way as the tip moved across the surface. This regular atomic structure makes it possible to clearly see the atomic lattice. It also makes surface features such as terraces and step edges easy to identify.

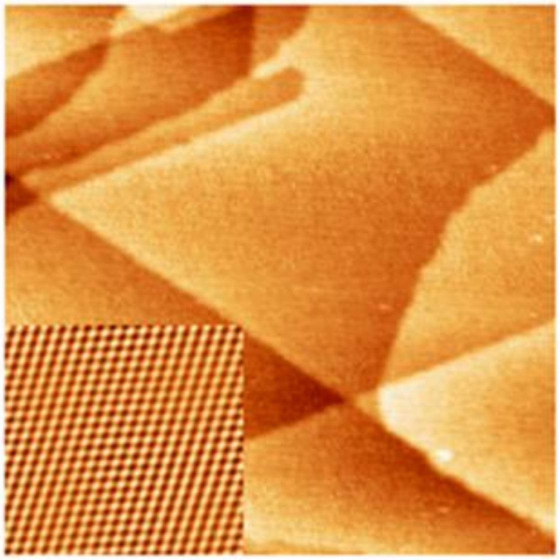

Figure 7. Constant-current STM image of Au(111), a single-crystalline surface. The main image (150 nm x 150 nm) shows flat terraces which are separated by clear step edges, while the corner image (5 nm x 5 nm) shows the regular atomic lattice, confirming the single-crystal structure. Figure taken from Ref. [7].

1.3. STM Imaging in Air

Until the mid-1990s, atomic resolution STM imaging was mostly done within a vacuum chamber where the contamination is reduced, and clean single-crystalline surfaces can be kept stable. Ultra-high vacuum conditions allow precise environment control. However, the downside to vacuum chambers is that they are sophisticated mechanically, expensive, and do not represent realistic environments. In 1995, A. M. Bittner, J. Wintterlin, B. Beran, and G. Ertl [8] extended STM imaging beyond vacuum conditions by studying bromine adsorption on different single-crystal platinum surfaces (Pt(111), Pt(100), and Pt(110)) both in air and in an electrolyte solution as shown in Figure 8. STM imaging in air relies on tunneling through a thin layer of molecules in the surrounding environment, which can affect image contrast but still allows atomic resolution under controlled conditions. In this setup, the STM tip and sample are immersed in an electrolyte solution. At the boundary between the electrode and the solution, tunneling occurs, and the current is influenced by the surrounding environment. The images that were obtained revealed how bromine atoms arranged themselves in an ordered, periodic lattice on the atomic level of each single-crystal surface. This work showed that STM can image atomic-scale surfaces outside of a vacuum.

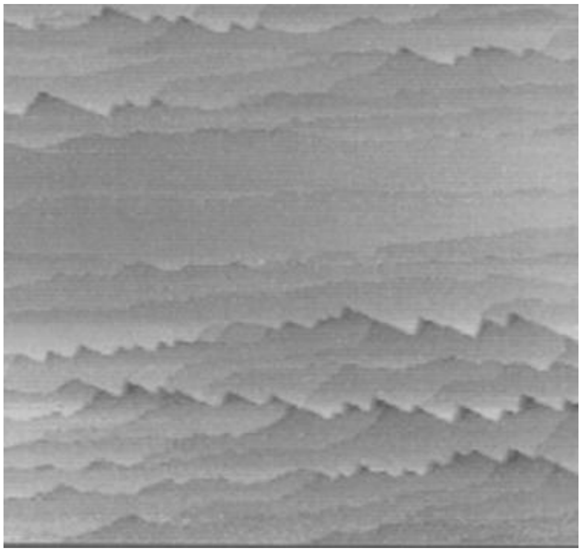

Figure 8. Constant-current STM image (5380 Å × 4970 Å) of Bromine adsorbed on Pt(100) surface taken in air. The image shows terrace and step structures of the Pt surface with bromine adsorbed across the surface. Figure taken from Ref. [8].

1.4. Poly Crystalline Structure

While single crystal surfaces provided ideal conditions for STM imaging, subsequent studies explored polycrystalline materials. In 1995, Kohei Uosaki, Ye Shen, and Toshihiro Kondo showed [9] that STM can be used to study a Highly ordered layer of Au (111) which was created on a polycrystalline gold substrate using vacuum deposition and heat treatment as shown in Figure 9. STM imaging revealed clear atomic steps and regular lattice patterns on this surface. From this they learned that polycrystalline materials can be studied at the atomic scale once the surface has been properly prepared. The STM has evolved from imaging single crystal structures to being a powerful tool used for studying well-ordered regions on otherwise disordered, polycrystalline surfaces.

Scanning tunneling microscopy has also been used to study polycrystalline materials in air. In one study [10], researchers used an STM to look at graphite grain boundaries. These images in Figure 10 revealed periodic atomic structures along the boundary between neighboring grains which allowed the grain boundary arrangement to be studied in detail. These results showed that the grain boundaries contain ordered and repeating atomic patterns rather than being disordered like previously thought.

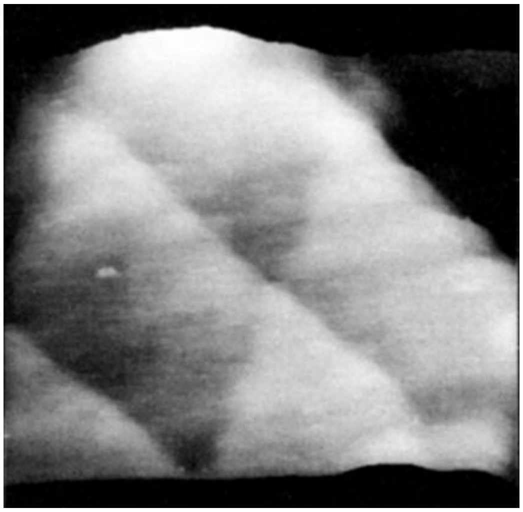

Figure 9. STM image (50 nm x 50 nm) of the Au(111) surface showing atomically flat terraces separated by step edges. The imaged region corresponds to a single grain of a polycrystalline substrate. Figure taken from Ref. [9].

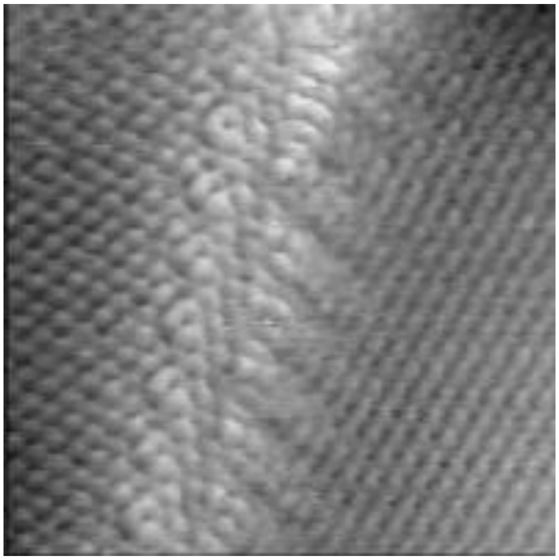

Figure 10. Polycrystalline STM image of graphite in air. (6 nm x 6 nm). Image shows clear atomic patterns withing each grain. The boundary can be seen where the atomic arrangement changes. This shows that boundaries have their own distinct order structure in air.

1.5. Tip Movement

1.5.1. Introduction

Achieving this level of detail, however, depends critically on precise control of the STM tip and careful surface preparation. Surface preparation determines what can and cannot be imaged by an STM. The ability to precisely position and control the tip determines whether atomic resolution can be achieved. Two types of motion are required to position the STM correctly. The tip of the STM needs to be brought within tunneling distance of the sample surface and this is done with course adjustment. Once the tip is brought within tunneling distance it must remain within several Angstrom of the surface. Since the tunneling current depends exponentially on the distance between the tip and the sample, even a small change can cause large variations in image quality. Different types of positioning mechanisms have been developed to decrease complexity and improve stability to achieve higher quality imaging.

1.5.2. Coarse Approach

The earliest form of course approach system used in an STM was the electrostatic walker seen in Figure 11. This mechanism uses a piezoelectric element supported by three small contacts that can be electrically clamped to a surface. By switching the voltages on these contacts while the piezo expands and contracts, the device moves forward in small steps, similar to a walking motion. The timing of the voltages and the structure of the device determine the step size and direction. This allows for nanometer-scale positioning while still enabling movement over several millimeters. However, the system is mechanically complex and requires precise control, making it sensitive to environmental changes. These limitations reduce its reliability and ease of use and led to the development of simpler approaches.

The next mechanism to be developed was the stick-slip slider shown in Figure 12. This simplified rough positioning is easier by using friction and inertia. When the piezo actuator slowly extends, static friction makes the slider move with it. When this happens it quickly contracts and inertia keeps the slider from moving back. This means that it keeps its motion headed in a forward direction. This type of mechanism is mechanically simple and capable of moving distances on the order of micrometers per step, making it applicable to a lot of different applications. The downside to this mechanism was its dependence on friction conditions and surface type. These factors heavily influenced the steps that were able to be taken and with what precision. This is a simpler mechanism than an electrostatic walker, but still heavily dependent on surface type.

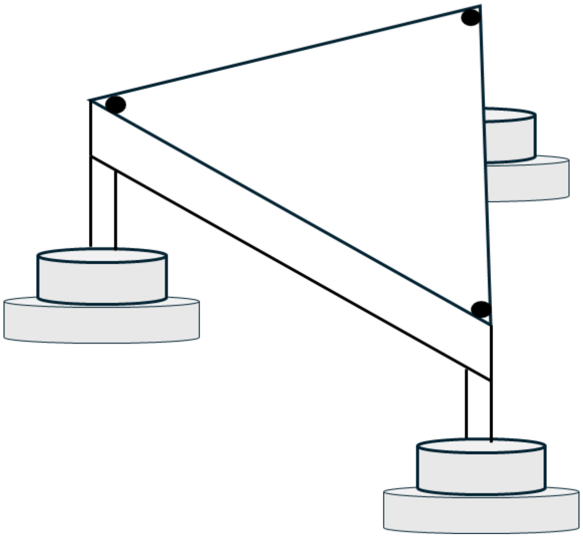

Figure 11. Electrostatic walker for course adjustment. Alternating electrostatic clamping and release of the legs produces stepwise motion, allowing the tip to “walk” toward the sample surface with nanometer-scale precision.

Since walker systems are sensitive, many designs use threaded screw for coarse positioning. The screw turns rotational motion into smooth linear movement. Threaded screws and stepper motors are simple for this type of application. They work reliably without the use of complex electronics. They are less precise and can cause small vibrations. However, regarding this application it does not matter. This mechanism is only needed to get the tip close enough for tunneling to occur so that a fine adjustment can be used to get it closer. This type of course adjustment is a reliable choice that is both simple and stable to be used for high resolution imaging. A challenge that arises with motorized course positioning is thermal drift. Thermal drift occurs when heat from the stepper motors or sample can shift the tip position by micrometers over the time it takes to scan the entire surface. This can be mitigated by allowing time for the system to reach thermal equilibrium or use motors that give off low amounts of energy in the form of heat.

1.5.3. Fine Approach

Once the tip is within tunneling distance, fine control systems are used to maintain atomic-scale positioning. A three-piezo-bar mechanism uses separate piezo actuators placed orthogonally to move in all three dimensions. This allows precise movements along each axis. However, the downside to this system is that it suffers from hysteresis and creep.

Hysteresis in piezo actuators occurs because the distance depends on the previous position, so the same voltage can produce slightly different motion each time. Creep occurs when a piezo actuator continues to move slowly even while the voltage is held constant. This is due to the gradual relaxation of the material over time. These limitations make the three-bar piezo system less suitable for maintaining the stable and precise positioning required for high resolution STM imaging.

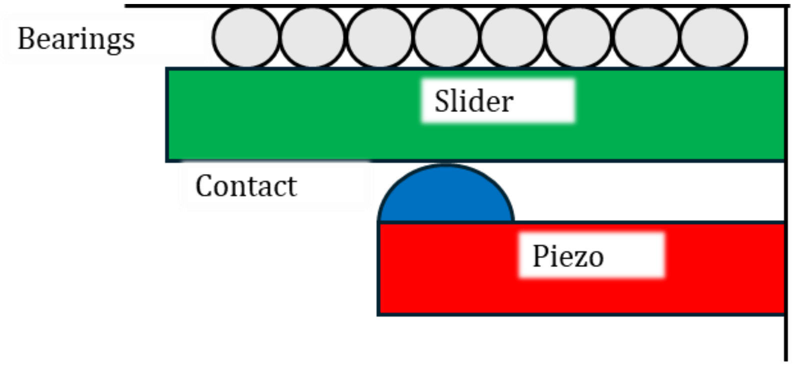

Figure 12. Schematic of a stick–slip slider for an STM. The red element is the piezoelectric actuator, the green block is the slider moving on bearings, and the blue region shows the contact where friction produces the stick–slip motion.

The next type of fine adjustment mechanism explored for the use of a STM was a flexure-based piezo mechanism. The main difference in this type of mechanism is the use of flexible elastic parts instead of sliding pieces. This eliminates friction and allows the parts to bend smoothly which results in precise and repeatable motion and constrains motion along a desired path. However, Flexure systems are often complex and only allow small movement range. The complicated structure also makes it difficult to set up and align and also still exhibit creep and hysteresis due to the piezo actuators.

A piezo buzzer actuator, which is shown in Figure 13, is the simpler option for fine positioning of the tip. This type of mechanism uses a thin piezoelectric disk that bends when a voltage is applied. By controlling the voltage that is applied to the disk, a wide array of movement can be produced. Piezo buzzers are cost effective, small in size, and mechanically simple, which make them easier to integrate than multi-bar flexure systems. The buzzer can also be electrically isolated into four different quadrants to achieve three-dimensional movement. Although they have a limited movement range, still exhibit creep and hysteresis, and require careful voltage control for smooth motion, their simple design and ability to move in multiple directions make them a good choice for fine STM tip adjustment where simplicity and ease of implementation are important.

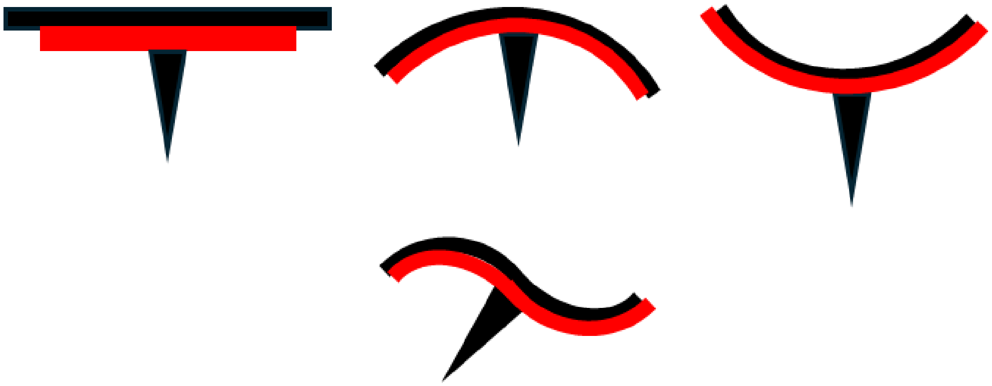

Figure 13. Piezoelectric buzzer actuator. The red piezoelectric ceramic is bonded to a black metal disc. When a voltage is applied, the ceramic changes its lateral dimensions, causing the combined structure to bend. This bending motion displaces the tip (triangle), allowing precise control of position.

Scanning tunneling microscopy is often associated with expensive equipment that is complex. However, it is possible to construct a fully functional STM using commercially available components. An example of this is Daniel Berard's home-built STM [10] shown in Figure 14. This work illustrates how functional STMs can be built using simple yet affective components while still achieving a high level of precision.

Course adjustment is achieved using a fine-threaded bolt, while fine tip positioning is controlled by a piezoelectric actuator. The sample holder is suspended on springs that help to reduce external vibrations. The system is controlled by a Teensy 4.1 microcontroller which handles the inputs and outputs. Because the Teensy's built-in DACs lack sufficient precision, external 20-bit DACs are used to drive the piezo actuator. The tunneling current is measured with a preamp that converts the current into a voltage, which is then digitized by an ADC for processing by the Teensy.

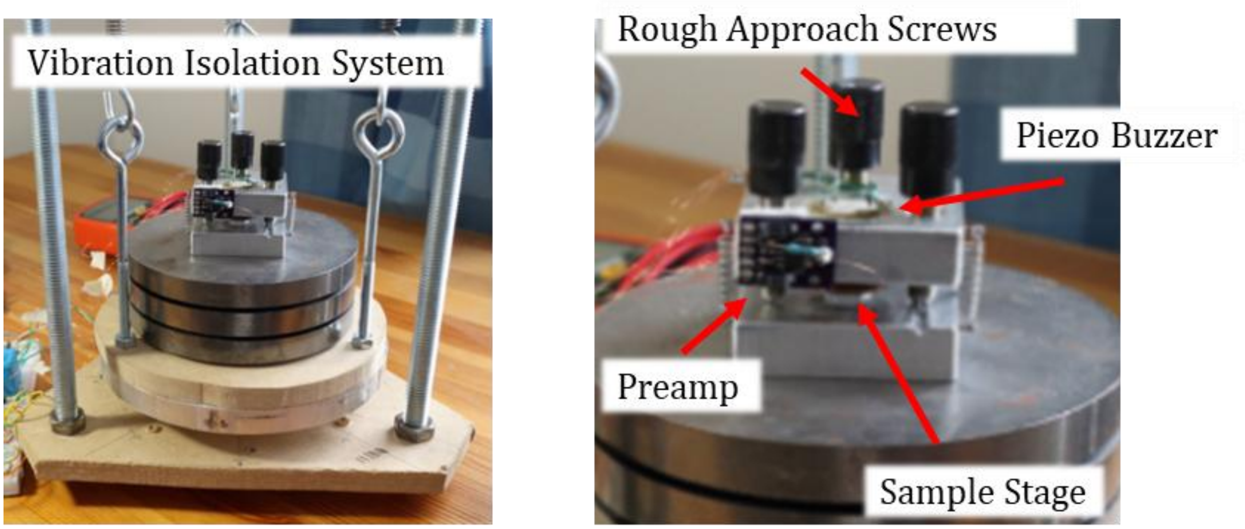

Figure 14. Photo of Daniel Berard’s home built STM featuring a vibration isolated system (left) and the zoomed in view of the STM (right). The STM consists of the rough approach screws for course adjustment, the piezo buzzer, the preamp, and the sample stage. Figure taken from Ref. [10].

1.6. Houghton STM

The Houghton University thin metal films lab currently houses a physical vapor deposition (PVD) chamber [11] which is used to create thin metal films. Once deposited, film thickness will be measured immediately using a phase stepping interferometer [12], and the crystal structure will be analyzed with an x-ray diffractometer (XRD) [13]. Houghton University is currently constructing a scanning tunneling microscope modeled after a design developed by Daniel Berard. This instrument will incorporate a dual-stage isolation platform with eddy current damping to reduce vibrations, as well as motorized control for an automated coarse approach. These features will enable stable, atomic-scale imaging of the thin metal films produced in the university’s thin films laboratory.

Chapter 2

QUANTUM MECHANICAL DESCRIPTION OF TUNNELING CURRENT

2.1. Schrodinger's Equation

The ability of the STM to create topographical scans of a substrate surface on an atomic level is enabled by the principles of a tunneling current. The tip and the sample are both at a fixed potential. This can be described by the potential energy function seen in Figure 15.

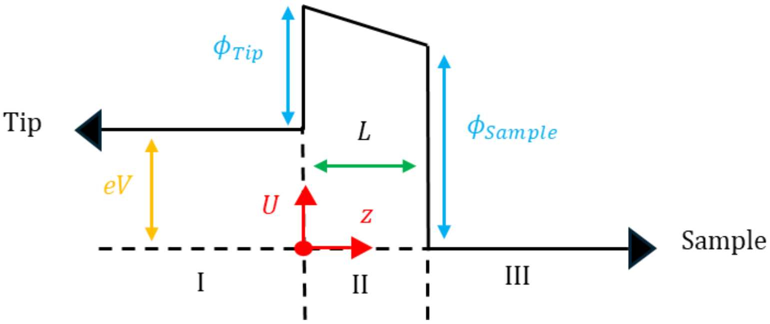

Figure 15. Potential energy $U(z)$ vs. position for an electron tunneling through a barrier of width L. The tip and sample work functions are denoted by ϕ_{tip} and ϕ_{sample}, respectively. A bias voltage V is applied such that the sample is at a higher electric potential than the tip. Because the electron carries charge $-e$, its potential energy is higher on the tip side by eV, resulting in a potential energy drop across the barrier.

The unique modern physics phenomenon that occurs when a moving particle encounters a barrier of finite height and length, such as an air gap, can be quantitatively described using the Wentzel-Kramers-Brillouin (WKB) approximation seen in Figure 16. This works to provide an estimate for the tunneling probability through a potential barrier by treating the wavefunction's exponential decay within the barrier. In classical mechanics, no current would flow if the electron's energy is less than the work function, but quantum mechanics allows tunneling through the barrier.

According to classical physics when a moving particle encounters this barrier the particle should be reflected. If a particle were to be in region II, then its kinetic energy would be negative which is not allowed under classical physics. U is the particle's potential energy and φ refers to the height of the potential barrier and dz refers to the width of the barrier.

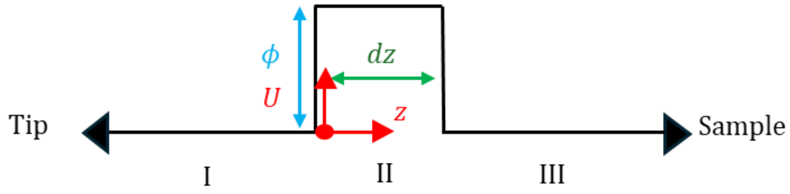

Figure 16. Illustration of the WKB approximation for electron tunneling. The potential energy barrier $U(z)$is approximated as a series of infinitesimally thin rectangular barriers of width dz . For each slice, the tunneling probability is calculated assuming a constant potential, and the total tunneling probability is obtained by combining contributions from all slices across the barrier.

Both regions II and III are off limits to a particle that is moving from the left to the right. However, according to quantum mechanics, the study of how matter has characteristics of both waves and particles, the particle has access to all three regions, regardless of its energy. This behavior can be understood through the concept of wave-particle duality. This is where electrons behave with both particle and wave properties. According to de Broglie's hypothesis, the wavelength of a particle is given by

$$\lambda = \frac{h}{p} \tag{1}$$

,

where h is Planck's constant and p is the momentum.

This leads to Schrodinger's energy equation

$$\frac{-\hbar^2}{2m}\frac{d^2\Psi}{dz^2} + U\Psi = E\Psi, \tag{2}$$

where $\hbar$ is $\frac{h}{2\pi}$ and m is the mass of an electron.

Rearranging this equation gives a second-order differential equation for the wave function

$$\frac{d^2\Psi}{dz^2} = \frac{-2m}{\hbar^2}\big(E - U(z)\big)\psi \equiv -k^2\Psi. \tag{3}$$

The form of the solution depends on the sign of k^2. In regions where k^2 is positive (region I), the solutions are oscillatory

$$\Psi_I = Ae^{ikz} + Be^{-ikz}, \tag{4}$$

where e^{ikz} is a right-traveling wave and e^{-ikz} is a left-traveling wave.

In Region III, the equation is the same as in Region I because the potential energy is zero in both regions ($U = 0$) and the total energy is conserved. Since we consider electrons incident from the left, there is no incoming wave from the right and therefore no reflected component in Region III. Thus, the wave function in this region is

$$\Psi_{III} = Fe^{ikz}. \tag{5}$$

Since the potential energy, U, is larger than the total energy, E, k must be imaginary to get a negative. Therefore, our equation becomes

$$\frac{d^2\Psi}{dz^2} = \frac{-2m}{\hbar^2}(E - U)\Psi \equiv \alpha^2\Psi. \tag{6}$$

We can now write the wave function for region II as

$$\Psi_{II} = Ce^{\alpha z} + De^{-\alpha z}, \tag{7}$$

which gives us our three wave functions needed to solve for our tunneling current.

Across the boundaries Ψ and $\frac{d\Psi}{dz}$ are continuous, so at the boundaries,

$$\Psi_I = \Psi_{II}\,, \tag{8}$$

$$\Psi_{II} = \Psi_{III}\,, \tag{9}$$

$$\frac{d\Psi_I}{dz} = \frac{d\Psi_{II}}{dz}, \tag{10}$$

$$\frac{d\Psi_{II}}{dz} = \frac{d\Psi_{III}}{dz}. \tag{11}$$

Applying the boundary conditions allows us to solve for the transmission coefficient. The square of the wavefunction represents the probability density, so $|A|^2$ corresponds to the density of electrons incident on the barrier, while $|F|^2$ corresponds to the density of electrons that have tunneled through it. Therefore, the ratio $\frac{|F|^2}{|A|^2}$ gives the probability that an electron approaching the barrier will be transmitted through it,

$$T = |\frac{F}{A}|^2. \tag{12}$$

Using our boundary conditions, we can solve our transmission coefficient to get four different equations. From the boundary at z = 0,

$$\mathrm{A + B = C + D} \tag{13}$$

and

$$ik(A - B) = \alpha(C - D). \tag{14}$$

From the boundary at z = dz,

$$Ce^{\alpha dz} + De^{-\alpha dz} = Fe^{ikdz} \tag{15}$$

and

$$\alpha(Ce^{\alpha dz} - De^{-\alpha dz}) = ikFe^{ikdz}. \tag{16}$$

Multiplying Equation (13) by ik and adding it to Equation (14) gives

$$2ikA = (ik + \alpha)C + (ik - \alpha)D\,. \tag{17}$$

The unknown constants C and D can be written in terms of F by multiplying Equation (15) by α and then either adding or subtracting from Equation (16), respectively to get

$$2\alpha C e^{\alpha dz} = F(\alpha + ik)e^{ikdz}, \tag{18}$$

and

$$2\alpha D e^{-\alpha dz} = F(\alpha - ik)e^{ikdz}. \tag{19}$$

Therefore, the ratio of outgoing electrons to incoming electrons is

$$\frac{F}{A} = [\frac{-k^2 + \alpha^2 + 2ik\alpha}{4ik\alpha} e^{ikdz} e^{-\alpha dz} + \frac{k^2 - \alpha^2 + 2ik\alpha}{4ik\alpha} e^{ikdz} e^{\alpha dz}]^{-1}. \tag{20}$$

Taking the magnitude squared and simplifying

$$|\frac{F}{A}|^2 = \{\frac{1}{16k^2\alpha^2}[(k^2 - \alpha^2)^2(e^{\alpha dz} - e^{-\alpha dz})^2 + 4k^2\alpha^2(e^{\alpha dz} + e^{-\alpha dz})^2]\}^{-1}. \tag{21}$$

The expression is rewritten in terms of hyperbolic functions using $\sinh(\theta)$ and $\cosh(\theta)$ identities

$$|\frac{F}{A}|^2 = \{\frac{1}{16k^2\alpha^2}[(k^2 - \alpha^2)^2 4\, sinh^2(\alpha dz) + 4k^2\alpha^2 4\, cosh^2(\alpha dz]\}^{-1}. \tag{22}$$

Trigonometric identities are then used to further simplify to get

$$|\frac{F}{A}|^2 = \{\frac{1}{4k^2\alpha^2}[(k^2 + \alpha^2)^2\, sinh^2(\alpha dz) + 4k^2\alpha^2]\}^{-1}. \tag{23}$$

Taking the modulus squared of the amplitude ratio gives the inverse transmission coefficient

$$T = [\frac{(k^2+\alpha^2)^2}{4k^2\alpha^2} sinh^2(\alpha dz) + 1]^{-1}. \tag{24}$$

We begin with the expression for the inverse transmission coefficient obtained from the boundary-condition solution

$$T = \{\frac{(k^2+\alpha^2)^2}{(2k\alpha)^2}\left[\frac{e^{\alpha dz} - \ e^{-\alpha dz}}{2}\right]^2 + 1\}^{-1}. \tag{25}$$

For a large tunneling distance where $\alpha dz \gg 1$, the exponential term $e^{\alpha dz}$ dominates. Using this approximation, the hyperbolic function is simplified by retaining only the dominant exponential contribution

$$T \xrightarrow[\alpha L\rightarrow\infty]{} 16(\frac{k\alpha}{k^2+\alpha^2})^2 e^{-2\alpha dz}. \tag{26}$$

,

Where

$$k^2 = \frac{2mE}{\hbar^2} \tag{27}$$

,

and

$$\alpha^2 = \frac{2m(\Phi - E)}{\hbar^2}. \tag{28}$$

The pre-exponential factor varies much slower than the exponential, so it can be treated as a constant, resulting in

$$T \ \approx \ T_0 e^{-2adz}. \tag{29}$$

Equation (29) gives the transmission coefficient for the barrier shown in Figure 16. The transmission coefficient for the barrier shown in Figure 15 can be approximated by dividing the barrier into an infinite number of infinitesimally thin slices and multiplying the corresponding transmission coefficients given by Equation (29). The barrier height is a function of z, where

$$\phi = \frac{\phi_{Sample} - \phi_{Tip} - eV}{L} z + \phi_{Tip}. \tag{30}$$

The resulting transmission coefficient is

$$T \approx T_0 e^{-2\frac{\sqrt{2m}}{\hbar}\int_0^L \sqrt{\left(\frac{\phi_{Sample}-\phi_{Tip}-eV}{L}z+\phi_{Tip}-E\right)}dz}. \tag{31}$$

Evaluating the integral gives

$$T \approx T_0 e^{-2\frac{\sqrt{2m}}{\hbar}\frac{2L}{3(\phi_{Sample}-\phi_{Tip}-eV)}[(\phi_{Sample}-E)^{3/2}-(\phi_{tip}-E)^{3/2}]}. \tag{32}$$

This can be simplified as

$$T \approx T_0 e^{-2\gamma L}, \tag{33}$$

where γ absorbs the constant in the exponent.

This transmission coefficient can be related to the tunneling current using time-dependent perturbation theory, which relates the tunnelling rate to transitions between states on either side of the barrier using Fermi's Golden Rule [14]

$$\Gamma_{i\to f} = \frac{2\pi}{\hbar} |< f|H'|i >|^2 \rho_f(E_f), \tag{34}$$

where H' is the perturbation Hamiltonian, i is the initial quantum state of the system, f is the final quantum state of the system after the transition, and ρ_f is the density of available final states at energy E_f.

The tunneling current can be described using

$$I = \frac{4\pi e}{\hbar}\sum_{t,s}|M_{ts}|^2 \delta(E_t - E_s)f(E_t)[1 - f(E_s)]. \tag{35}$$

Here M_{ts}describes the tunneling between a tip state $t$and a sample state s, and the factor of 4 accounts for spin degeneracy. The functions $f(E_t)$ and $1 - f(E_s)$ are Fermi–Dirac probabilities that ensure the tip state is occupied, and the sample state is empty for tunneling to occur. The Dirac delta function $\delta(E_t - E_s)$ enforces energy conservation, meaning electrons only tunnel between states of equal energy, where $E_t$and $E_s$are the energies in the tip and sample respectively.

The summation over discrete states is approximated by an integral using the density of states. This is an approximation in which the discrete energy levels are treated as a continuous spectrum, since in macroscopic systems the spacing between energy levels is extremely small where

$$\sum_t \to \int dE_t \rho_t(E_t) \tag{36}$$

and

$$\sum_s \to \int dE_s \rho_s(E_s). \tag{37}$$

The current can now be written with integrals rather than summations as

$$I = \frac{4\pi e}{\hbar}\int_{-\infty}^{\infty}\int_{-\infty}^{\infty} dE_t dE_s \rho_t(E_t)\rho_s(E_s)|M_{ts}|^2\delta(E_t - E_s)f(E_t)[1 - f(E_s)]. \tag{38}$$

because of the Dirac Delta function, the first integral should set $E_t = E_s$. The applied voltage introduces a complication here because the density of states and fermi functions are both defined with respect to the fermi energy of that particular metal. Therefore, in order to set the tip and sample energies equal to each other, we must set $E_t = E - eV$ and $E_s = E$, resulting in a tunneling current of

$$I = \frac{4\pi e}{\hbar}\int_{-\infty}^{\infty} dE \rho_t(E - eV)\rho_s(E)|M_{ts}|^2 f(E - eV)[1 - f(E)]. \tag{39}$$

It is important to note that a small bias voltage $V$is applied between the tip and the sample, and that we are working at reasonably low temperatures. In this situation, the Fermi–Dirac distributions are well approximated as step functions, meaning states below the Fermi energy are occupied $(f \approx 1)$ and those above are empty $(f \approx 0)$. As a result, only the electronic states within an energy window of width eVaround the Fermi level contribute to tunneling. This restricts energy integration to a small range of size eV. Over this narrow interval, the tunneling matrix, which is proportional to the transmission coefficient, element $|\ M(E)\ |^2$ and the densities of states of the tip and sample vary only slowly with energy, so they can be treated as approximately constant and taken outside the integral. Putting all of this together, the approximate tunneling current is

$$I \approx \rho_t(E - eV)\rho_s(E)|M_{ts}|^2 \int_{E_F - eV}^{E_F} dE. \tag{40}$$

The integral and the tunneling matrix leads to the simplified form

$$I \propto \rho_t(E - eV)\rho_s(E)e^{-2\gamma L}\mathrm{V}. \tag{41}$$

The assumption can then be made that the density of states of the tip does not change much as the tip scans over the sample surface, which gives

$$I \propto V\rho_s(E)e^{-2\gamma L}. \tag{42}$$

This shows that the tunneling current depends on three main things: the applied voltage, the sample's density of states, and the distance between the tip and sample. The current increases with voltage because more electrons can tunnel and it reflects the sample's density of states. Most importantly, the current depends exponentially on the separation distance between the tip and the sample.

Chapter 3

INSTRUMENTATION AND ELCTRONIC DESIGN

3.1. Physical Structure

The entire mechanical system is shown in Figure 17. The vibrations damping system is made up of a 1.27 cm thick Al plate and four 1.27 cm thick Al rings. The outer springs have a spring constant of 29.77 N/m while the inner springs have spring constant of 52.54 N/m. The scan head and sample stage are both connected to the vibration damping system, with the sample stage bolted to the isolation system as shown in Figure 18. The sample stage is a 1.27 cm thick Al plate, containing three 2.54 cm holes to accommodate the 1/4-80, 4" long threaded rods attached to the stepper motors. Each motor is mounted to the stage using M3 x 4 mm screws. The sample rests on a stationary sample stage. The Al scan head, which contains the piezo buzzer, STM tip, and preamplifier, moves relative to the sample stage.

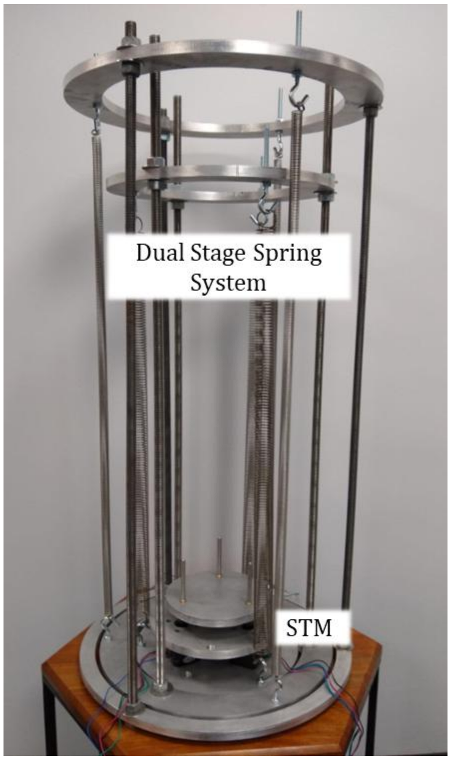

Figure 17. Vibration isolation system used to hold scan head and sample stage.

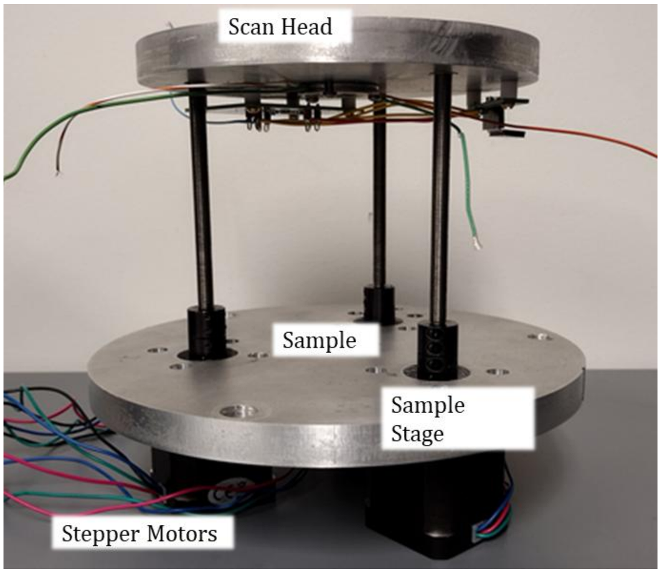

Figure 18. Sample stage with stepper motors bolted onto the stage. Shaft couplings connect the motor axles to 1/4-80, 4" long threaded rods, which are threaded into inserts glued into holes in the scanning head. The ends of the threaded rods were machined on a lathe to remove the threads, allowing for a more secure fit within the shaft couplings. The sample will sit on the center of the sample stage.

The scan head, shown in Figure 19, which is made of a 1.27 cm thick Al plate has a preamplifier mounted to it using a dual in-line package (DIP) board. This allows the preamplifier, the piezo buzzer, and the rest of the circuit to be electrically connected. The scanning tip is to be mounted directly onto the piezo buzzer. For the piezo electrode to be electrically insulated from the scanning tip, a small piece of ceramic is placed between the two. The buzzer is divided into four electrically isolated quadrants Figure 20. By applying a voltage to different sections of the buzzer, it can bend to create horizontal movement. When a voltage is applied evenly across the disk it moves vertically. This precise, multi-directional movement is achieved with just one small actuator which keeps the design simple yet precise. The quadrants are split up as follows: (z+x), (z+y), (z-x), and (z-y).

3.2. Sending Voltages

Coarse adjustment of the STM tip position is achieved using stepper motors, which bring the tip into proximity with the sample surface. The Teensy 4.1 microcontroller shown in Figure 21 serves as the main electrical control component of the STM, communicating with the MAX5719AGSD+, 20-bit, digital-to-analog converters (DACs) and ADC via the serial peripheral interface (SPI) protocol to control and monitor the voltages required for operation.

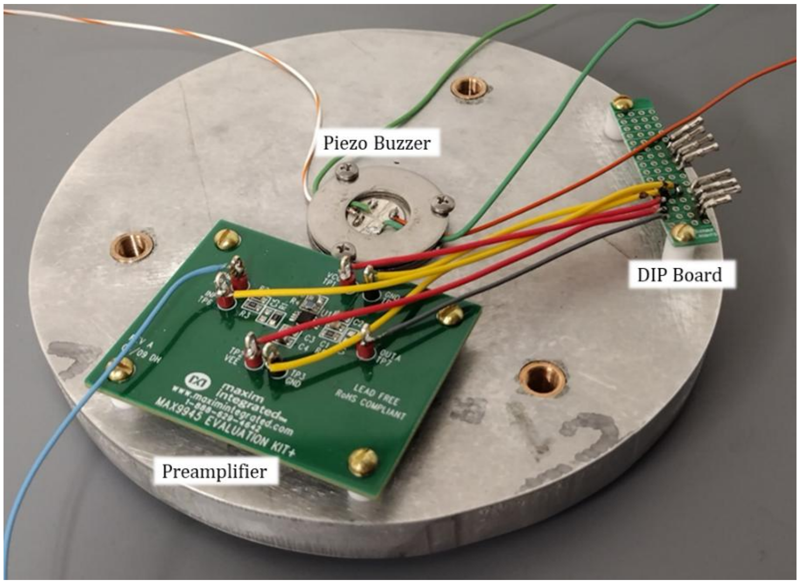

Figure 19. STM drilled and tapped scan head. Preamplifier, DIP board, and piezo buzzer for fine adjustment. Scan head has been removed from the mounting rods.

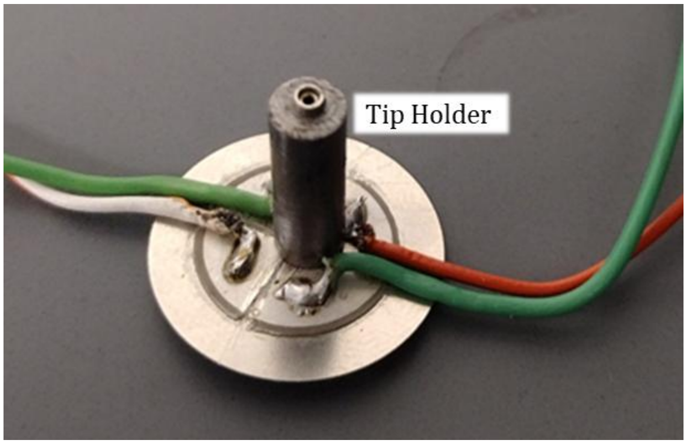

Figure 20. Electrically insulated 4-quadrant piezo buzzer. Tip holder is a stainless-steel rod with a hole drilled and a female pin connector for the STM tip.

The Teensy also functions to send control signals to multiple digital-to-analog converters (DACs) shown in Figure 22, which generate analog voltages for the rest of the system. The circuit shown in Figure 24 takes the output of each DAC and adds and subtracts them via operational amplifiers (op-amps) to produce the buzzer quadrant voltages. Fine adjustment is then performed using a piezoelectric actuator, which enables precise positioning during operation. A bias voltage is applied to the STM tip to generate a tunneling current between the tip and the sample surface.

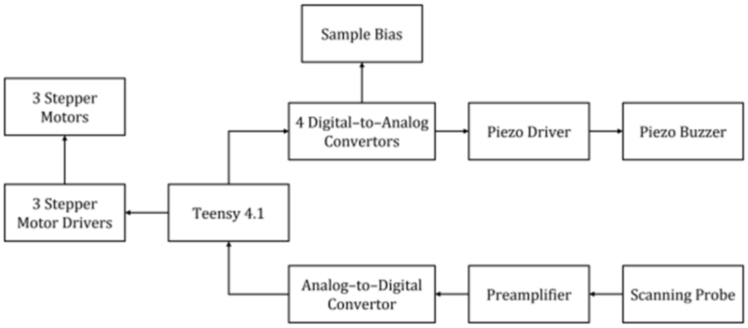

Figure 21. Electronics flow chart showing Teensy 4.1 microcontroller at the center of the electronics.

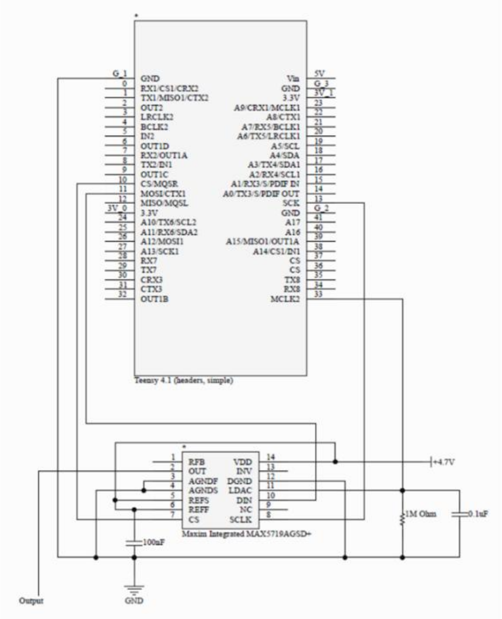

Figure 22. DAC connection to the Teensy 4.1 via the SPI protocol, with each DAC's chip select (CS) pin connected to a separate digital pin on the Teensy.

The stepper motors provide the coarse positioning which is required to bring the STM tip close to the sample surface. This system uses three stepper motors that move independently of one another and move the scan head relative to the sample stage. Once the tip is sufficiently close to the surface, fine adjustments can be made using the piezoelectric buzzer. The stepper motor drivers shown in Figure 23 , rather than the motors themselves, are connected to the Teensy 4.1 microcontroller. Because the Teensy operates at 3.3 V logic levels while the stepper motor drivers require 5 V inputs, an SN74ACT244N buffer is used to perform level shifting between the two. The buffered signals are then sent to the TB6600 stepper motor drivers, which control the operation of the stepper motors.

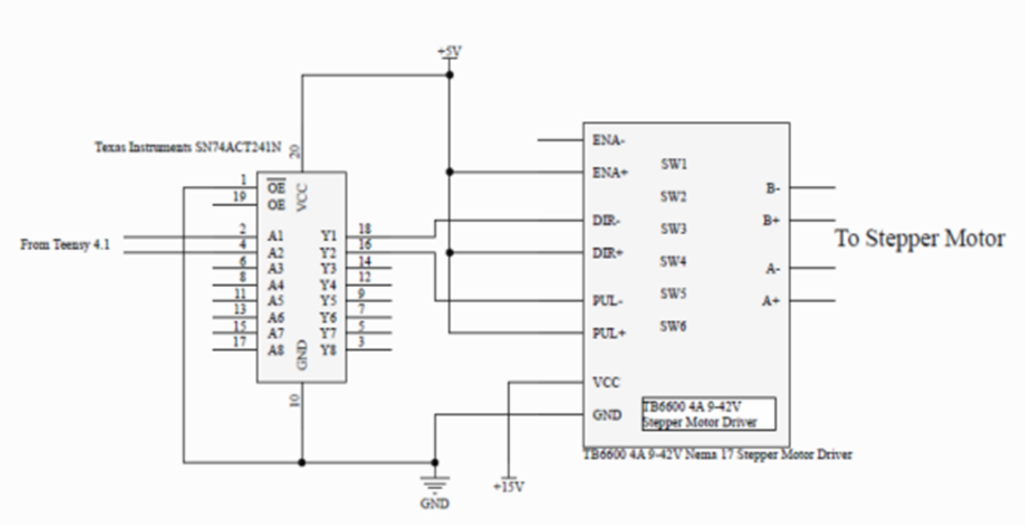

Figure 23. Stepper motor circuit which shows the connection from the Teensy 4.1 microcontroller to the stepper motor driver and then to the stepper motor.

3.3. *Receiving Data*

The preamplifier, MAX9945 Evaluation Kit+ board shown in Figure 25, consists of an operational amplifier with a 100 MΩ feedback resistor connected between the output and the negative input, which is also connected to the STM tip. A small capacitor is placed in parallel with the resistor to reduce voltage spikes and improve circuit stability. Additional capacitors are connected between power inputs and ground to stabilize the power supplies, and the positive input of the operational amplifier gets connected to ground.

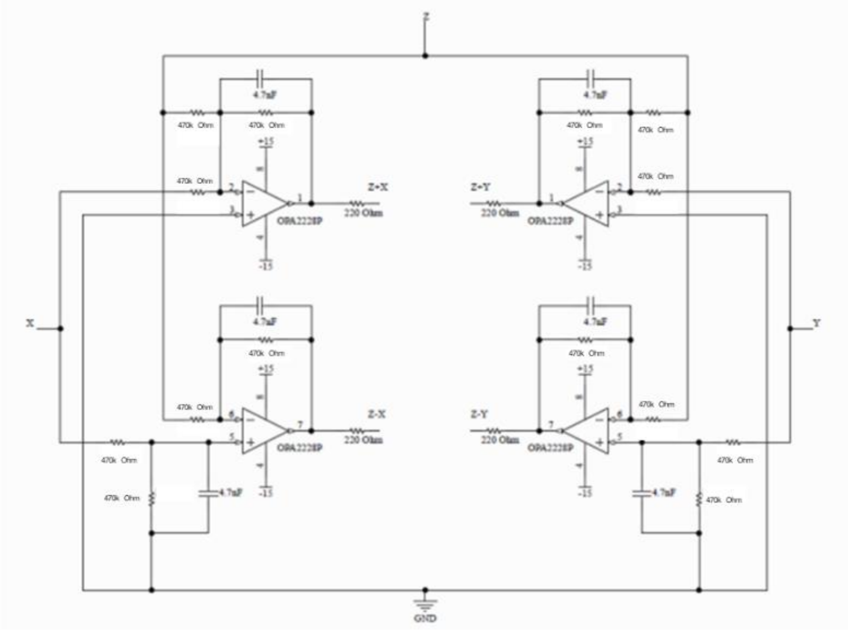

Figure 24. Piezo driver circuit where outputs of DACs (X, Y, Z) are added and subtracted via op-amps to create the four directional movements for the piezo buzzer.

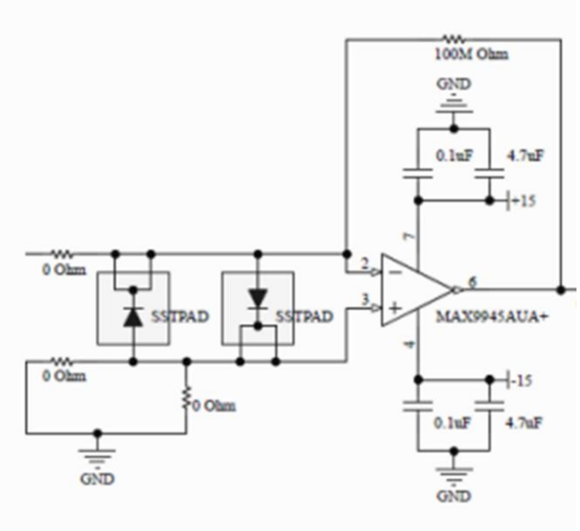

Figure 25. Preamplifier circuit using the MAX9945 operational amplifier with 100 MΩ feedback and stabilization capacitors.

The circuit shown in Figure 26 is used to measure the tunneling current produced between the STM tip and sample surface. The tunneling current is converted by a preamplifier into a voltage signal ranging from −18 to 18 V. This voltage is then digitized by an, ADS8691, 18-

bit, analog-to-digital converter (ADC), which converts the signal into a 20-bit value and transfers it to the Teensy 4.1 via the SPI protocol for further processing.

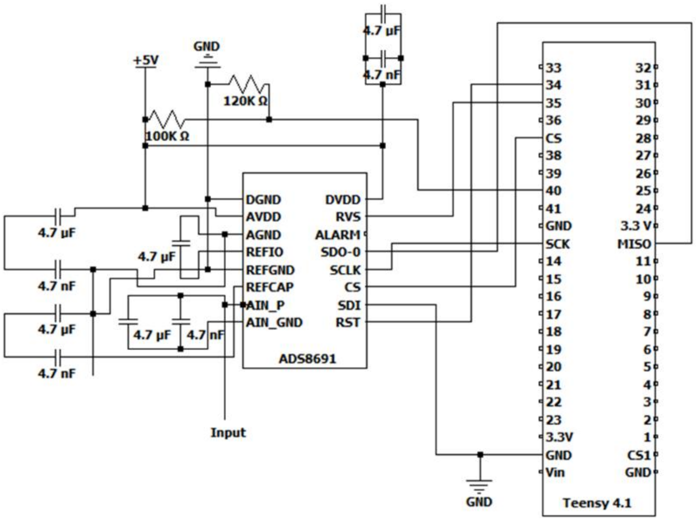

Figure 26. ADC connections to Teensy 4.1 microcontroller with decoupling capacitors to reduce noise.

Chapter 4

EXPERIMENTAL RESULTS

4.1. Overview

The STM system consists of stepper motors, DACs, a piezoelectric actuator, a preamplifier, and an ADC. The stepper motors handle coarse positioning and are controlled by the Teensy 4.1 through a buffer and motor drivers. The DACs translate digital commands from the Teensy into analog voltages that drive the piezo for fine positioning. The preamplifier conditions the tunneling signal, which is then converted into a digital value by the ADC and sent back to the Teensy. Each component was tested on its own and then as part of the full system to verify correct operation.

4.2. Stepper Motor

The stepper motors are controlled using the Teensy 4.1 microcontroller. The Teensy 4.1 sends a control signal to a buffer, which converts the 3.3 V logic level used by the Teensy to the 5 V logic level required by the digital inputs of the motor drivers. This signal is then sent from the buffer to the stepper motor driver which drives the stepper motors. The stepper motors were tested independently of one another first. The motors were tested by programming the Teensy 4.1 to send a specific number of step pulses corresponding to a predetermined rotation angle. The resulting displacement was then measured and compared to the expected value to verify accurate motor operation. Once it was verified that each motor was working independently then all the motors were tested together. Initially, the Teensy 4.1 generated identical step pulse sequences for each motor, causing each motor to complete its full number of steps sequentially before the next motor was activated. However, for our application we need each motor to make one rotation and then move on to the next motor. This was tested with a 2 second timing delay to ensure that each motor rotated before the next. The timing delay was then removed so the transition happened quickly enough that it was not a visible difference. To ensure that each motor was rotating the correct amount, a piece of tape was placed on the end of the threaded bolt so that a measurement could be made from that point.

4.3. *Digital to Analog Converter*

The digital to analog converters (DAC) were tested independently of one another. The DACs were then tested as one sending unit. The DACs have a 5 V power supply and are controlled via the serial peripheral interface (SPI). The 8 most significant bits of the input data were varied from 0 to 255, while the remaining 12 bits were held at 0. This input corresponds to the voltage output of the DACs. This output range is between 0 -5V. A linear trend can be seen between SPI value and the DAC output voltage in Figure 27.

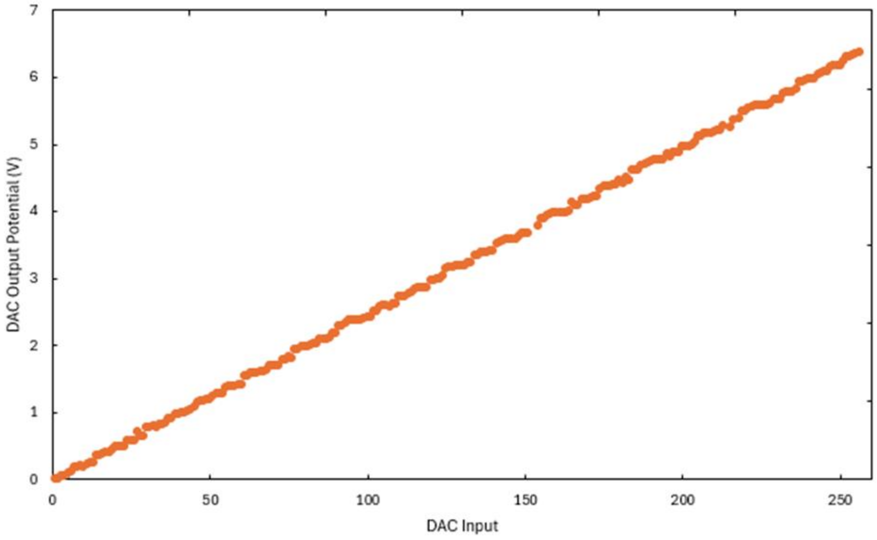

Figure 27. DAC output voltage based on SPI value from Teensy 4.1 microcontroller, with the output potential relative to ground. The output voltage was read into the Teensy's analog input, which has a resolution of 5V / 1024.

4.4. *Piezo Buzzer*

The piezo driver circuit produces four outputs, corresponding to the four quadrants of the piezo buzzer. The operational amplifiers were powered with a positive 15 V and a negative 15 V. Each initial input (X, Y, and Z in Figure 24) was controlled by its own power supply as seen in Table 1. The output was then measured using a multimeter on each of the four quadrants of the piezo buzzer. The test was verified by comparing the measured values to the predicted results, which showed consistent agreement.

Table 1. Piezo buzzer test results in volts. Based on the three different outputs of the DAC's which are the inputs for the piezo driver circuit. Op-amps flip the voltages to be negative, but this was neglected for simplicity.

X	Y	Z	Z + X	Z - X	Z + Y	Z - Y
0	0	0	0	0	0	0
0	0	1	1	1	1	1
1	1	1	2	0	2	0
1	1	2	3	1	3	1
2	2	1	3	-1	3	-1
0	1	0	0	0	1	-1
4	0	0	4	-4	0	0
2	2	2	4	0	4	0
3	1	2	5	-1	3	1

4.5. Analog to Digital Converter

The analog-to-digital converter (ADC) converts the input voltage from the preamplifier into a digital value transmitted to the Teensy 4.1 via SPI. Although the ADC has a 20- bit resolution, only the 8 most significant bits were used in this experiment, resulting in an effective 8-bit range (0–255). The ADC was tested over an input range of 0–3 V using a power supply, and nine different input voltages were applied. The resulting output showed a linear relationship; however, the data is offset upward, since 0 V should correspond to a value of approximately 128 for a −20 V to +20 V input range as seen in Figure 28.

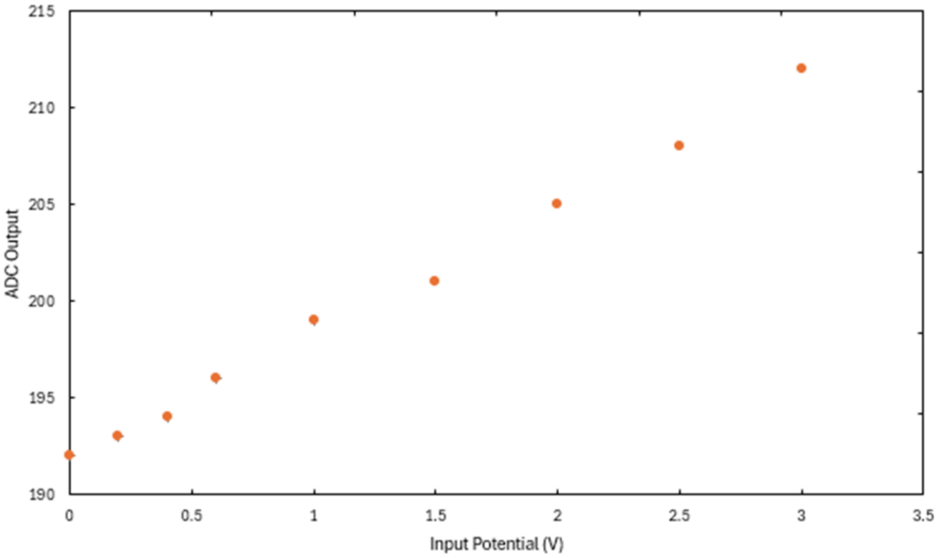

Figure 28. ADC output values based on input potential received from the preamplifier, with the input potential relative to ground. This graph correctly shows the linear relationship between input potential and ADC output. The discrepancy in the graph is due to the limited range of ADC output values.

Chapter 5

CONCLUSIONS AND FUTURE WORK

The construction of our STM is currently a work in progress. Most of the electrical wiring and core circuitry have already been completed. The DAC, ADC, and microcontroller-based system have been successfully used and tested independently of one another. They have demonstrated correct signal generation, acquisition, and communication via SPI. The remaining work focuses on integrating and finalizing the system. The updated circuit needs to be mounted onto the main breadboard and fully incorporate all the electronics on it. The physical apparatus is mostly complete but needs to be finished and aligned. Once finished, the electronic and mechanical systems can be incorporated together. Additional remaining work includes finalizing the control software for coordinated operation of the system and constructing a housing to reduce the effects of air currents from the ventilation system.

References

---

[1] K. Bian, C. Gerber, A. J. Heinrich, D. J. Müller, S. Scheuring, and Y. Jiang, "Scanning probe microscopy," *Nat. Rev. Methods Primers* **1**, 36 (2021).
[2] G. Binnig and H. Rohrer, "Surface studies by scanning tunneling microscopy," *Surface Sci.* **126**, 236–244 (1983).
[3] G. Binnig and H. Rohrer, "Scanning tunneling microscopy—from birth to adolescence," *Rev. Mod. Phys.* **59**, 615–625 (1987).
[4] "The Nobel Prize in Physics 1986: Gerd Binnig, Heinrich Rohrer," *NobelPrize.org*, https://www.nobelprize.org/prizes/physics/1986/summary/ (accessed January 28, 2026).
[5] H. A. Sodano and J.-S. Bae, "Eddy current damping in structures," *Shock Vib. Dig.* **36**, 469–478 (2004).
[6] R. Wiesendanger, H.-J. Güntherodt, G. Güntherodt, R. J. Gambino, and R. Ruf, "Observation of vacuum tunneling of spin-polarized electrons with the scanning tunneling microscope," *Phys. Rev. Lett.* **65**, 247–250 (1990).
[7] H. Wolfschmidt, C. Baier, S. Gsell, M. Fischer, M. Schreck, and U. Stimming, "STM, SECPM, AFM and electrochemistry on single crystalline surfaces," *Materials* **3**, 4196–4213 (2010).
[8] A. M. Bittner, J. Wintterlin, and G. Ertl, "Bromine adsorption on Pt(111), (100), and (110) — an STM study in air and in electrolyte," *Surface Sci.* **335**, 291–299 (1995).
[9] K. Uosaki, Y. Shen, and T. Kondo, "Preparation of a highly ordered Au(111) phase on a polycrystalline gold substrate by vacuum deposition and its characterization by XRD, GISXRD, STM/AFM, and electrochemical measurements," *J. Phys. Chem.* **99**, 14117–14122 (1995).
[10] D. Berard, *Home-Built STM*, https://dberard.com/home-built-stm/ (accessed January 28, 2026).
[11] M. D. Bowman, "Thin metal film physical vapor deposition system," *B.S. thesis*, Houghton University (2023).
[12] L. Yelle, "Houghton University's phase-shifting laser interferometer for the study of thin metal films," *B.S. thesis*, Houghton University (2025).
[13] O. D. Fall, "Constructing an X-ray diffractometer for the analysis of thin metal films at Houghton University," *B.S. thesis*, Houghton University (2025).
[14] D. Jena, "Fermi's Golden Rule," Physics of Semiconductors and Nanostructures (ECE 4070/MSE 5470 lecture notes), Cornell University, 2015. https://courses.cit.cornell.edu/mse5470/2015_ece4070_mse5470_primernotes_fermigoldenrule_dj.pdf (accessed May 1, 2026).